Radiometric framework for image mosaicking

Anatoly Litvinov and Yoav Y. Schechner

Department of Electrical Engineering, Technion—Israel Institute of Technology, Haifa 32000, Israel

Nonuniform exposures often affect imaging systems, e.g., owing to vignetting. Moreover, the sensor's radiometric response may be nonlinear. These characteristics hinder photometric measurements. They are particularly annoying in image mosaicking, in which images are stitched to enhance the field of view. Mosaics suffer from seams stemming from radiometric inconsistencies between raw images. Prior methods feathered the seams but did not address their root cause. We handle these problems in a unified framework. We suggest a method for simultaneously estimating the radiometric response and the camera nonuniformity, based on a frame sequence acquired during camera motion. The estimated functions are then compensated for. This permits image mosaicking, in which no seams are apparent. There is no need to resort to dedicated seam-feathering methods. Fundamental ambiguities associated with this estimation problem are stated. © 2005 Optical Society of America

OCIS codes: 100.3190, 100.3020, 110.0110, 350.2660, 150.0150, 040.1490.

1. INTRODUCTION

Imaging systems are prone to problems stemming from nonuniform irradiance of the detector plane and from a nonlinear response of the sensor. The first problem is optical: Owing to vignetting and foreshortening,[1] the sensor periphery is not illuminated as intensely as its center. The second problem is electronic: The light signal is translated into a weak electric signal, which is then amplified prior to being sent to the camera output or storage. This amplifier may not be linear. Moreover, a nonlinear response may partly be due to special optical components in the imaging system.[2,3] These phenomena should be compensated, if quantitative photometric measurements are sought on the basis of the image data.

A particular application in which these effects are apparent is *image mosaicking*.[4] Mosaicking is a common method to obtain a wide field-of-view (FOV) image of a scene. Images are captured as a camera moves and are then stitched together to obtain an extended image. Mosaicking has been used extensively in various scientific fields.[7–9,11–17] Typically, a radiometric mismatch exists between the different frames, owing to the above-mentioned problems. This results in seams in the stitched image mosaic. Various methods were developed to feather the seams[12,18–20] or camouflage them[10] in scene edges. However, those pure image-processing methods address the perceptual effects of seams rather than accounting for the root cause of the mismatch.

Apparently, these problems can be solved in the optical level: Had the imaging system been perfect, radiometric inconsistencies would not have occurred. However, even an inconsistency of 1% is noticeable in 8-bit sensors (and certainly in higher-sensitivity sensors). Moreover, humans can easily detect such minute radiometric errors, as demonstrated in Fig. 1. Hence this utopian line of thought may pose impractical tolerances on the optical engineering process. For this reason, image nonuniformities and sensor nonlinearities are a fact of life. Moreover, some-

times spatial nonuniformities can be of benefit, since they can improve the dynamic range of the imaging system.[21–23] In particular, this was demonstrated by *generalized mosaicking*[22,23]: Scene points that are saturated in some frames become unsaturated in others, thanks to the spatial nonuniformity of the system (Fig. 2). In the past, however, generalized mosaicking was limited to cameras having a linear radiometric response or at least a known response.

Nonuniformities and sensor nonlinearly can be compensated for if they are carefully precalibrated. A standard calibration process, however, may not always be practical. For example, in zoom lenses the nonuniformities should be measured for all possible zoom, focus, and aperture settings. In addition, the performance of the camera (in particular its electronics) may somewhat degrade over long periods of time, especially in harsh environments. Moreover, calibration equipment may not be available or affordable to all.

For these reasons, in this paper we propose a hybrid solution to the problem. It combines computer-vision tools with a model that accounts for the physical processes occurring in the imaging system. The nonuniformity and nonlinearity are blindly self-calibrated on the basis of ordinary scenes, as part of the mission the imaging system is designed to do. The situation analyzed is such that an unknown optical nonuniformity exists in the imaging system, as well as an unknown nonlinear radiometric response. We then suggest a method for simultaneously estimating both of them.

In addition, we discuss fundamental ambiguities associated with our estimation problem. In spite of these ambiguities, the method is able to compensate for the image nonuniformity, such that all the resulting images are mutually consistent. Hence the output value of a scene point is the same (excluding random noise), whether it is imaged at the center of a frame or at the periphery of a frame. The compensation for the nonuniformity and non-
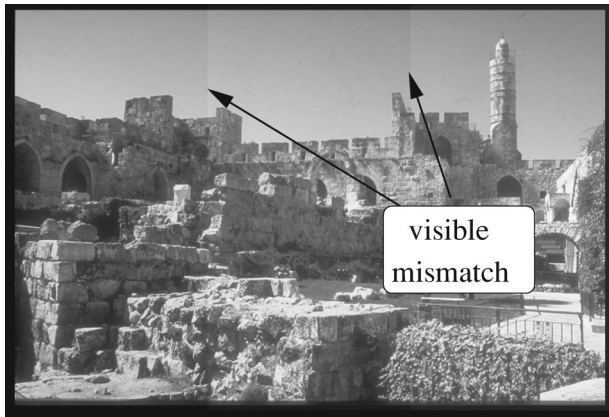
Fig. 1. Illustrating human sensitivity to radiometric mismatch. Several consecutive image parts were biased by 4% with respect to each other, as if stitched by a process of mosaicking. Even such a small mismatch creates clear visual artifacts.
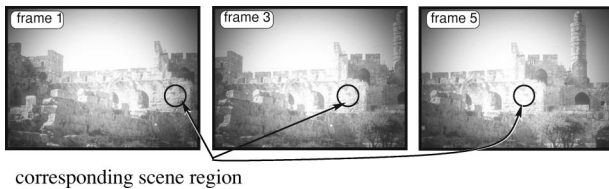

Fig. 2. Several frames from a simulated image sequence acquired by a camera with optical nonuniformity. Owing to the nonuniformity, each scene point is acquired with a different optical setting. The selected region is saturated in frame 5 and not saturated in frames 1 and 3.

linearity yields images that are equivalent to the scene radiance. We then use the outputs corresponding to different frames to construct wide FOV image mosaics. The compensation quality is sufficiently high to practically eliminate the visibility of seams in mosaics without resorting to dedicated seam-removal techniques.

We note that studies have been carried out with the aim of estimating the radiometric response function by using known temporal variations of exposure.[24,25] On the basis of those studies, methods for estimating the radiometric response, by using unknown temporal variations of exposure[26–28] or gain[29,30] were developed. There are analogies between these studies and our work, because optical nonuniformity in a moving camera has an effect similar to temporal variation of exposure. However, Refs. 26,30,31 are based on parametric models of the radiometric response. In contrast, it is demonstrated in this work that it is possible to estimate the radiometric response and the optical nonuniformity without prior parametric models. The ambiguities involved in our estimation problem are analogous to those determined by Grossberg and Nayer[32] (with regard to methods that use temporal variations of exposure[25,26,28,30,31]). Nevertheless, we show that these ambiguities can be solved with very little *a priori* knowledge of either the camera non uniformity or the radiometric response function.

This work may be related to methods designed for thermal infrared imaging. Nonuniformity correction (NUC) algorithms have been devised to handle fixed pattern noise caused by pixel-dependent sensitivities to thermal radiation. Analogous to our method, recent nonuniformity correction algorithms have been scene based and exploited image motion[33–36]; however, these studies are different from ours. Existing NUC algorithms for thermal sensors assume a linear radiometric response with spatially varying bias. On the other hand, our work handles general nonlinear radiometric response functions and, in addition, exploits the spatial correlations of nonuniformities caused by optical transfer.

2. STATEMENT OF THE PROBLEM

Consider a system in which the irradiance at the detector plane is spatially varying, when the scene radiance is uniform. This can happen because of vignetting, foreshortening, or lens distortions (Fig. 3). This spatially varying optical response is denoted $M(\mathbf{x})$, where $\mathbf{x}=(x,y)$ is a location vector in the local coordinate system of the frame, where $\mathbf{x} \in [1,N]^2$. Here N denotes the number of pixels along each transversal axis of the detector array. We define $\tilde{I}(\mathbf{x})=M(\mathbf{x})I(\mathbf{x})$ as the irradiance falling on the camera detector, accounting for the spatial variation. Here I is the irradiance falling on the camera detector when $M=1$. The irradiance falling on the detector is converted into an electric signal via the camera amplifier, which has a radiometric response $r(I)$. The radiometric function is generally nonlinear,[24–27,31,32,37,38] usually owing to properties of electronic amplifiers. Alternatively, in image intensifiers, nonlinearity can stem from the response of the phosphors[39] of the intensifying tube.

The gray-level value v in pixel $\mathbf{x}$ is

$$v(\mathbf{x}) = r\left[\tilde{I}(\mathbf{x})\right] = r[M(\mathbf{x})I(\mathbf{x})]. \tag{1}$$

The range of gray-level values in the detector is $v \in [0,v_{\max}]$, where $v_{\max}=255$ for 8-bit digital cameras.

Suppose that the radiometric response function $r(I)$ and the optical nonuniformity $M(\mathbf{x})$ of this system are unknown. Our goal is to estimate these unknown functions. Consequently, we aim to estimate the image irradiance I with high dynamic range and in a wide FOV. The questions we pose are the following:

1. Can this estimation problem be solved on the basis of an image sequence taken for mosaicking?
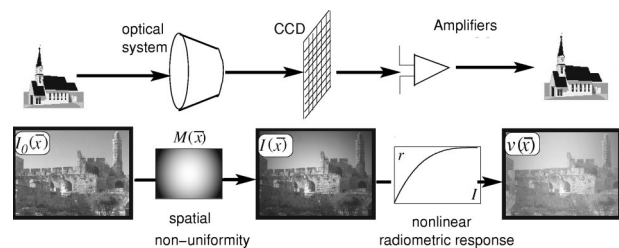2. What are the fundamental limitations of this estimation?

Fig. 3. Imaging system model. The optical system induces spatial inhomogeneities on the image, which are characterized by $M(\mathbf{x})$. The camera electronics has an unknown radiometric response $r(I)$.

3. Can this estimation be good enough to create seamless image mosaics without resorting to feathering techniques?

3. SOLUTION

A. Fundamental Equation
Typically, the radiometric response function of the camera r is monotonic.[40] Therefore r is invertible, and hence we can write

$$r^{-1}[v(\mathbf{x})] = \tilde{I}(\mathbf{x}) = M(\mathbf{x})I(\mathbf{x}). \qquad (2)$$

Thus

$$\log\{r^{-1}[v(\mathbf{x})]\} = \log[M(\mathbf{x})] + \log[I(\mathbf{x})]. \qquad (3)$$

We define the functions $g[v(\mathbf{x})] \equiv \log\{r^{-1}[v(\mathbf{x})]\}$ and $l(\mathbf{x}) \equiv \log[M(\mathbf{x})]$. Equation (3) is then

$$g\left[v(\mathbf{x}_p^{f_0})\right] = l(\mathbf{x}_p^{f_0}) + \log(I), \qquad (4)$$

where $\mathbf{x}_p^{f_0}$ denotes the pixel in frame f_0 onto which a scene point p is imaged.

Owing to camera motion, the same scene point is measured in frame f_1 at image pixel $\mathbf{x}_p^{f_1}$. We assume that the scene is static during the acquisition of the sequence. Thus the radiance at scene points does not change in time. This allows us to compare measurements across frames. Particularly, the scene point analyzed in Eq. (4) yields

$$g\left[v(\mathbf{x}_p^{f_1})\right] = l(\mathbf{x}_p^{f_1}) + \log(I). \qquad (5)$$

Assume that the image registration process[8,16,20,22,30,41–45] is successful, i.e., that corresponding image pixels are registered. We define

$$Q\left[v(\mathbf{x}_p^{f_0}),v(\mathbf{x}_p^{f_1}),\mathbf{x}_p^{f_0},\mathbf{x}_p^{f_1}\right] \equiv g\left[v(\mathbf{x}_p^{f_0})\right] - g\left[v(\mathbf{x}_p^{f_1})\right]$$
$$- l(\mathbf{x}_p^{f_0}) + l(\mathbf{x}_p^{f_1}). \qquad (6)$$

According to Eqs. (4) and (5), we should obtain

$$Q\left[v(\mathbf{x}_p^{f_0}),v(\mathbf{x}_p^{f_1}),\mathbf{x}_p^{f_0},\mathbf{x}_p^{f_1}\right] = 0. \qquad (7)$$

This is the basic equation on which we further develop our analysis. We note that at this stage there is no need for accurate registration. The reason is that for the recovery of g and l we may decide to include only points that reside on smooth image regions, discarding pixels in proximity to edges. On the basis of Eqs. (6) and (7), we aim to calculate g and l simultaneously, subsequently deriving r, M, and I.

B. Least-Squares Formalism
In this subsection we formulate the least-squares optimization equations for estimation of $g(v)$ and $l(\mathbf{x})$. The ranges of v and $\mathbf{x}$ are discrete and finite. Hence the ranges of $g(v)$ and $l(\mathbf{x})$ are finite and discrete as well. Let P be the number of registered scene points, which are arbitrarily chosen, and let F be the number of frames. We denote by $\mathbf{x}_p^f$ the location of a specific scene point p in frame f, in the coordinate system of f. We define an error function Ψ_0 on the basis of Eqs. (6) and (7):

$$\Psi_0 = \sum_{p=1}^{P}\sum_{f=1}^{F-1}\sum_{e=f+1}^{F} Q^2\left[v(\mathbf{x}_p^f),v(\mathbf{x}_p^e),\mathbf{x}_p^f,\mathbf{x}_p^e\right]$$
$$+ \lambda_g\sum_{v=0}^{v_{max}} g''(v)^2 + \lambda_l\sum_{x=1}^{N}\sum_{y=1}^{N}\left[\nabla^2 l(\mathbf{x})\right]^2. \qquad (8)$$

The first sum in Eq. (8) penalizes for violation of Eq. (7). The second and third sums are regularizing terms, which require smoothness of the functions. The regularization seeks to minimize the second derivations of $g(v)$ and $l(\mathbf{x})$. We use the following approximations of second derivatives:

$$g''(v) \equiv g(v-1) - 2g(v) + g(v+1), \qquad (9)$$

$$\nabla^2 l(\mathbf{x}) \equiv l(x-1,y) + l(x,y-1) - 4l(x,y)$$
$$+ l(x+1,y) + l(x,y+1). \qquad (10)$$

The parameters λ_g and λ_l are weights of the regularization terms, relative to the data-fitting term. Equation (8) treats correspondences across the entire image sequence. That is, our estimation problem is not based solely on correspondences between consecutive frames, in contrast to Refs. 26,30. Therefore we expect this method to be more robust.

Measurements of low gray-level values have high relative uncertainty due to noise. Thus we want to increase the relative weight of measurements [Eqs. (6) and (7)] corresponding to high gray-level values v. For this purpose we use a weighted error function

$$\Psi_1 = \sum_{p=1}^{P}\sum_{f=1}^{F-1}\sum_{e=f+1}^{F} w^2\left[v(\mathbf{x}_p^f),v(\mathbf{x}_p^e)\right]Q^2\left[v(\mathbf{x}_p^f),v(\mathbf{x}_p^e),\mathbf{x}_p^f,\mathbf{x}_p^e\right]$$
$$+ \lambda_g\sum_{v=0}^{v_{max}} g''(v)^2 + \lambda_l\sum_{x=1}^{N}\sum_{y=1}^{N}\left[\nabla^2 l(\mathbf{x})\right]^2. \qquad (11)$$

For any two readout values v_1 and v_2, we defined the weight function as

$$w(v_1,v_2) = \frac{v_1 v_2}{(v_1^2 + v_2^2)^{1/2}}. \qquad (12)$$

For a detailed explanation for this choice of weighting, see Appendix A. We seek $\hat{g}(v)$ and $\hat{l}(\mathbf{x})$ that minimize Ψ_1.

The solution somewhat depends on the values of λ_g and λ_l used. This issue is common in optimization processes that include regularization terms. The effect of regularization depends on the amount of data versus the number of unknown variables. When we have enough data in the form of Eq. (7), low values of λ_g and λ_l can be used. Using values for λ_g and λ_l that are too low may result in fluctuations in $g(v)$ and $l(\mathbf{x})$.

C. Avoiding a Trivial Solution
Interestingly, any two constant functions $g(v)=\text{const}_1$ and $l(\mathbf{x})=\text{const}_2$ satisfy Eq. (7), yielding $\Psi_1=0$ in Eq. (11). A constant $g(v)$ implies $r^{-1}(v)=I_0$, where I_0 is a constant. This is a nonphysical solution for the radiometric response function, because in this case $r(I)$ is not defined for the full range of I but, rather, only for a single value. It is clear that this class of solutions is not a desired one. To

avoid it, we can make a minor assumption: Assume that, in one local domain of v, the radiometric response function of $r(v)$ is linear; thus also $r^{-1}(v)$ is linear in that range. Let us denote the boundaries of this domain as v_{start} and v_{end}; then, for this local domain,

$$\frac{\partial r^{-1}}{\partial v} = r^{-1}(v+1) - r^{-1}(v) = k, \qquad (13)$$

where k is a slope of r^{-1}. The choice of the slope is arbitrary, as long as $k > 0$ (for monotonically increasing radiometric functions). Denote the irradiance correspondents to $r^{-1}(v_{\text{start}})$ by I_{start}. Then

$$r^{-1}(v) = (v - v_{\text{start}})k + I_{\text{start}}, \qquad (14)$$

for $v \in [v_{\text{start}}, v_{\text{end}}]$. The error function Ψ is then

$$\Psi = \Psi_1 + \lambda_m \sum_{v=v_{\text{start}}}^{v_{\text{end}}} \{g(v) - \log[(v - v_{\text{start}})k + I_{\text{start}}]\}^2. \qquad (15)$$

The parameter λ_m weights this local linearity requirement. As with k, the value I_{start} is arbitrarily chosen, offsetting the solution of $g(v)$. The aspect of offsets is addressed in Section 4. We select v_{start} and v_{end} as being a few gray levels apart, around the middle of the gray-scale range.

D. Matrix Formulation
In this subsection we describe a simple method for obtaining the solution by using a matrix formulation. Let us organize $M(\mathbf{x})$ in a column-stack vector and denote the vector by $M(\tilde{x})$, where the scalar $\tilde{x}$ corresponds to the vector $\mathbf{x}$. This vector is of length $\tilde{N} = N^2$. Tracking some of the scene points in several images provides many linear equations such as Eq. (7). This set of equations can be written as

$$\mathbf{Rs} = \mathbf{0}, \qquad (16)$$

where

$$\mathbf{s} = \begin{pmatrix} \mathbf{g} \\ \mathbf{l} \end{pmatrix} \qquad (17)$$

is the sought solution, composed of

$$\mathbf{g} = [g(0), \dots g(v_{\text{max}})]^T, \qquad \mathbf{l} = [l(1), \dots l(\tilde{N})]^T. \qquad (18)$$

The matrix $\mathbf{R}$ is sparse. In each row n, the nonzero elements of $\mathbf{R}$ are determined as follows:

$$\mathbf{R}[n, v(\mathbf{x}_p^{f_0})] = -\mathbf{R}[n, v(\mathbf{x}_p^{f_1})] = 1,$$

$$-\mathbf{R}(n, \tilde{x}_p^{f_0}) = \mathbf{R}(n, \tilde{x}_p^{f_1}) = 1, \qquad (19)$$

where $\mathbf{x}_p^{f_0}$ and $\mathbf{x}_p^{f_1}$ are pixels corresponding to the same scene point p as seen in different frames f_0 and f_1. The matrix $\mathbf{R}$ is of dimensions $E \times O$, where E is the number of equations of the form of Eqs. (6) and (7) and $O = v_{\text{max}} + \tilde{N}$ is the length of the vector $\mathbf{s}$.

To accommodate the weighting described in Eqs. (11) and (12), we define the diagonal matrix $\mathbf{W}$ of size $E \times E$. Any element on the diagonal is of the form

$$\mathbf{W}(n,n) = w[v(\mathbf{x}_p^{f_0}), v(\mathbf{x}_p^{f_1})], \qquad (20)$$

where w is defined in Eq. (12). Note that each element $\mathbf{W}(n,n)$ varies according to the values of the intensities used in the corresponding row n of $\mathbf{R}$.

For regularization, we add matrix rows expressing second-order derivatives of g and l. We use the common approximation for the one-dimensional (1D) second-derivative operator:

$$\tilde{\mathbf{D}} = \begin{bmatrix} 1 & -2 & 1 & 0 & \dots & \dots & \dots & \dots & \dots & \dots \\ 0 & 1 & -2 & 1 & 0 & \dots & \dots & \dots & \dots & \dots \\ \vdots & & & & & & & & & \vdots \\ 0 & \dots & \dots & \dots & \dots & \dots & 0 & 1 & -2 & 1 \end{bmatrix}. \qquad (21)$$

We also use the common approximation for the two-dimensional (2D) Laplacian operator, which is a generalization of Eq. (21). This 2D operator is denoted by $\tilde{\mathbf{L}}$ and is a sparse matrix of dimensions $\tilde{N} \times \tilde{N}$. For details about the mathematical expression of $\tilde{\mathbf{L}}$, see Appendix B.

We then define an operator on $\mathbf{s}$, which effectively operates the second-order derivative on $g(v)$, as

$$\mathbf{D}_g = [\tilde{\mathbf{D}}_{v_{\text{max}}} \quad \mathbf{0}_{\tilde{N}}], \qquad (22)$$

where $\tilde{\mathbf{D}}_{v_{\text{max}}}$ is of the form of Eq. (21), with dimensions $(v_{\text{max}} - 2) \times v_{\text{max}}$. Here $\mathbf{0}_{\tilde{N}}$ is a zero matrix of size $(v_{\text{max}} - 2) \times \tilde{N}$. As for the spatial smoothness of $l(\tilde{x})$, we define an operator on $\mathbf{s}$, which effectively operates the 2D Laplacian over $l(\tilde{x})$, as

$$\mathbf{D}_l = [\mathbf{0}_{v_{\text{max}}} \quad \tilde{\mathbf{L}}], \qquad (23)$$

where $\mathbf{0}_{v_{\text{max}}}$ is a zero matrix of size $\tilde{N} \times v_{\text{max}}$.

Combining Eqs. (19), (20), (22), and (23) results in an overconstrained system of equations. We seek the least-squares solution of this system,

$$\hat{\mathbf{s}} = \arg\min_{s}(\mathbf{s}^t \mathbf{A}^t \mathbf{A} \mathbf{s}), \qquad (24)$$

where

$$\mathbf{A} = \begin{bmatrix} \mathbf{WR} \\ \lambda_g \mathbf{D}_g \\ \lambda_l \mathbf{D}_l \end{bmatrix}. \qquad (25)$$

This is achieved by singular-value decomposition (SVD). SVD yields multiple solution vectors. Some vectors correspond to a zero singular value and represent the trivial solution described in Subsection 3.C. When these vectors are excluded, the sought solution is the vector corresponding to the smallest singular value.[46] This solution undergoes several transformations, which are described in Section 4.

Let us assume now that $M(\mathbf{x})$ is a 1D function over the domain $(1 \dots \tilde{N})$. As examples, we note two cases to which this 1D model applies. In the first case, the nonuniformity varies only along the x axis, and thus $N = N$. In the second case, $M(\mathbf{x})$ is isotropic; i.e., it changes only as a function of the radius ρ from the center of the frame. In this case, $\tilde{N} = N/\sqrt{2}$. In both cases, the number of unknown values of

l is much smaller than N^2, and, for this reason, it is much easier to solve the problem numerically.

In the 1D model we do not need to use the operator $\tilde{\mathbf{L}}$ in Eq. (23) to regularize $l(\mathbf{x})$. Rather, we use in Eq. (23) the matrix $\tilde{\mathbf{D}}$, defined in Eq. (21),

$$\mathbf{D}_l = \left[\mathbf{0}_{v_{\max}} \ \ \tilde{\mathbf{D}}_{\tilde{N}} \right], \qquad (26)$$

where $\tilde{\mathbf{D}}_{\tilde{N}}$ is of the form of Eq. (21), with dimensions $(\tilde{N} - 2) \times \tilde{N}$.

4. FUNDAMENTAL AMBIGUITIES

In this section we describe ambiguities that are fundamental to the problem. These ambiguities exist in every method attempting to blindly estimate the radiometric response function $r(I)$ in conjunction with the optical nonuniformity $M(x)$. These ambiguities are analogous to those that appear when $r(I)$ is estimated in conjunction with exposure times.[32] Let us take a closer look at Eqs. (6) and (7). We denote by $g(v)$ and $l(x)$ the functions derived from the true radiometric response and the true optical nonuniformity. Together, they form the vector $\mathbf{s}$ and satisfy Eqs. (7) and (16). Let c_g and c_l be arbitrary constant offsets. Interestingly, $\hat{g} = g(v) + c_g$ and $\hat{l} = l(x) + c_l$ satisfy Eq. (16) as well. Therefore we cannot determine from the data what the true offsets are. To alleviate this ambiguity, we set $\max[r(I)] = 1$ and $\max[M(x)] = 1$. We should note that this setting does not affect the appearance of the image but only its global brightness scale.

In addition, the solution suffers from an exponential ambiguity. If $\mathbf{s}$ is a true solution satisfying Eq. (16), then $K\mathbf{s}$ satisfies Eq. (16) as well. K is an arbitrary scale factor. Hence $\hat{g}(v) = Kg(v)$ and $\hat{l}(x) = Kl(x)$ are legitimate solutions. Thus

$$\hat{r}^{-1}(v) = \exp[\hat{g}(v)] = \exp[Kg(v)] = \left[r^{-1}(v) \right]^K, \qquad (27)$$

and

$$\hat{M}(x) = \exp[\hat{l}(x)] = \exp[Kl(x)] = \left[M(x) \right]^K. \qquad (28)$$

Since K is arbitrary, the solution is ambiguous.

5. IRRADIANCE ESTIMATION

We will now describe how the ambiguities described in Section 4 influence the estimation of image irradiance. On the basis of the estimated spatial and radiometric functions [Eqs. (27) and (28)], we express the estimated irradiance value $\hat{I}$ by using Eq. (2):

$$\hat{I} = \frac{[r^{-1}(v)]^K}{[M(\mathbf{x})]^K} = I^K. \qquad (29)$$

This means that we may err in estimating the true value of the image irradiance by this exponential ambiguity.

Note that K in Eq. (29) behaves exactly like a γ-correction operation. To appreciate the significance of this result, recall that the entire analysis had not assumed any parametric form for the response function. Thanks to the process we performed, the problem became much simpler: Now it is a parameterized problem, with only a *single parameter* that needs to be estimated for full recovery of the irradiance. It is interesting to see that no matter what the original response function is, the intensity resulting from the estimation is γ distorted, at most.

This exponential ambiguity is not severe in applications that do not require quantitative photometric measurements. Such applications include display for human interpretation. In these cases, recall that the user can tune the display γ correction for visual plausibility, and therefore there is no need to determine K a priori.

A simple way to disambiguate the solution is to define a criterion for image quality and then optimize it as a function of K. Reference 37 presents a blind gamma-estimation method based on minimization of high-order frequency correlation. Another suitable criterion can be image entropy, to be maximized. This is the criterion we used in the experiments described in Section 7. For quantitative photometric measurements, we can alleviate the ambiguity by using minor *a priori* knowledge of either the camera nonuniformity or of the radiometric response function. In particular, knowledge of system transmittance $M(\mathbf{x})$ at two distinct pixels is sufficient to disambiguate the result. Then the unknown parameter K can be calculated.

6. DATA FUSION

We now describe the method for estimating the irradiance of each mosaic point, given its multiple corresponding measurements. More explanations are described in Ref. 23. Let a measured intensity readout at a point be $v(\mathbf{x})$ with uncertainty $\Delta v(\mathbf{x})$. The estimated optical nonuniformity is $\hat{M}(\mathbf{x})$, and the estimated radiometric response function is $\hat{r}$. Compensating for the nonuniformity, we find that the image irradiance in frame f is

$$I_f = \frac{\hat{r}^{-1}[v(\mathbf{x})]}{\hat{M}(\mathbf{x})}, \qquad (30)$$

and its uncertainty is

$$\Delta I_f = \left| \frac{\partial I_f}{\partial v(\mathbf{x})} \Delta v(\mathbf{x}) \right|. \qquad (31)$$

We let the readout uncertainty be $\Delta v(\mathbf{x}) = 0.5$, since the intensity readout values are integers. In saturated pixels the uncertainty is very high; thus their corresponding $\Delta v(\mathbf{x})$ is set to be a very large number. Pixels are considered saturated if their value $v(\mathbf{x})$ is very close to the camera saturation limit, e.g., to 255 for an 8-bit detector.[23] We estimate the irradiance as

$$\hat{I} = \widehat{\Delta I}^2 \sum_f \frac{I_f}{\Delta I_f^2}, \qquad (32)$$

where

$$\widehat{\Delta I} = \left(\sum_f \frac{1}{\Delta I_f^2} \right)^{-1/2}. \qquad (33)$$

Equation (32) is the maximum-likelihood estimation of I, if the measurements I_f are Gaussian and independent.

Fig. 4. Images created with the filter $M(\mathbf{x})$ and the radiometric response function $r(I)$. Scene features become darker toward the frame periphery.

7. EXPERIMENTS

To demonstrate our method, we performed simulations as well as experiments based on real data. First, we describe the simulations and then the results of experiments.

A. Simulations

To create a sequence of simulated images, we took a wide FOV image and divided it into a sequence of small frames. Each frame was multiplied by a known nonuniform function $M(\mathbf{x})$, which simulates a vignetting effect. In our examples, we simulated 1D variations, in which nonuniformity varies only along the x axis. We used the resulting frames as inputs to a simulated radiometric response function $r(I)$. Finally, we added to each image $v(\mathbf{x})$ independent white Gaussian noise having a standard deviation of 2.5 gray levels. Figure 4 shows several images that were created by this process, where $M(x) = \exp[-(x/200)^2]$ and $r(I) = I^{0.45}$. Here x denotes the horizontal coordinate relative to the frame center, in units of pixels. Subsequently, $g(v) = \log[r^{-1}(v)]$ and $l(x) = \log[M(x)]$ are defined. Both $g(v)$ and $l(x)$ create the vector $\mathbf{s}$ according to Eq. (17). The solid curve in Fig. 5 plots $r^{-1}(v)$ and $M(x)$.

We used the synthetic image sequence to estimate the vector $\hat{\mathbf{s}}$. First, the matrix $\mathbf{R}$ was created according to Eqs. (19). To impose smoothness, the Laplacian operators for $g(v)$ and $l(x)$ were formulated. We estimated $\hat{\mathbf{s}}$ according to Eq. (24). We chose moderate values of λ_g and λ_l that were sufficient for avoiding fluctuations in the solution. According to Section 4, we expected an ambiguity in our solution. For display purposes only, we alleviated this ambiguity by manually multiplying $\hat{\mathbf{s}}$ by a global factor, such that its plot is comparable with the plot of $\mathbf{s}$. The dashed curve in Fig. 5 plots $\hat{r}^{-1}(v)$ and $\hat{M}(x)$, and it shows that the estimated $\hat{\mathbf{s}}$ closely matches the original vector $\mathbf{s}$, except for the said ambiguity.

On the basis of $\hat{\mathbf{s}}$, we extracted the functions $\hat{r}(I)$ and $\hat{M}(x)$, and, on the basis of them, we then fused the frames into a mosaic, as described in Section 6. Figure 6 shows the final image mosaic that was derived from the simu-

lated image sequence, samples of which are shown in Fig. 4. Note that no seams appear in Fig. 6, although we have not performed any process dedicated to seam removal. In contrast, Fig. 7 shows an image mosaic produced without accounting for the radiometric distortions. That mosaic contains seams. It is possible to remove those seams by known feathering methods. However, we have demonstrated that there is no need for such a process, since in Fig. 6 we obtained a seamless mosaic without using feathering. We have also checked our algorithm by using vari-
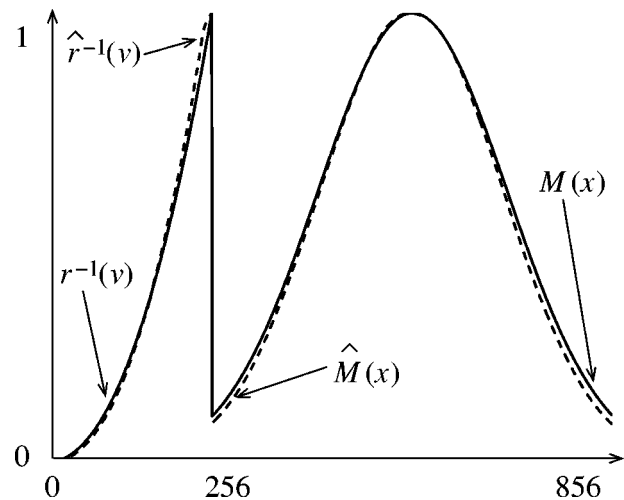

Fig. 5. Solid curve, the true inverted radiometric response function $r^{-1}(v)$ and the true nonuniformity function $M(\mathbf{x})$. Both functions are concatenated. Dashed curve, the estimated solution $\hat{r}^{-1}(v)$ and $\hat{M}(\mathbf{x})$ (concatenated).

Fig. 6. Image mosaic constructed in the simulation. No seams appear in the mosaic, although the original images suffered from an unknown vignetting, and the recovered vignetting and radiometric response erred by an exponential function. No dedicated seam-removal method was applied.

Fig. 7. Image mosaic constructed by direct stitching without compensating for the radiometric response function $r(I)$ and the optical nonuniformity $M(\mathbf{x})$.
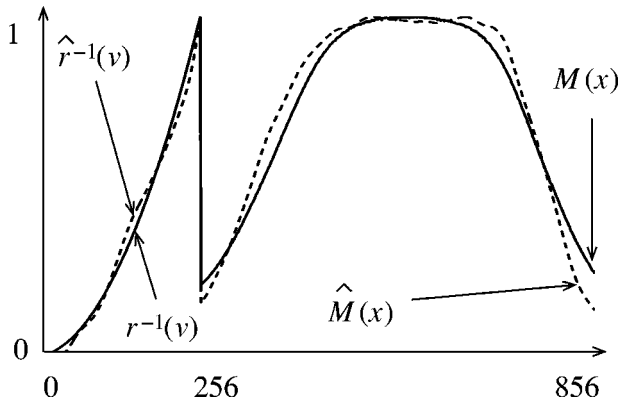
Fig. 8. Experiment that uses real data. Solid curve, the true inverted radiometric response function $r^{-1}(v)$ and the true nonuniform function $M(\mathbf{x})$. Both functions are concatenated. Dashed curve, the estimated solution $\hat{r}^{-1}(v)$ and $\hat{M}(\mathbf{x})$ (concatenated).
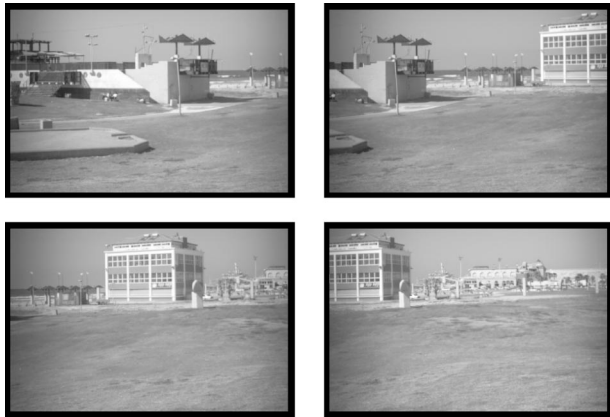

Fig. 9. Image frames sampled from a sequence acquired by a Nikon D100 digital camera. A spatially varying optical filter had been attached to the camera lens. Scene features become darker toward the periphery of each frame.

ous other functions for the optical nonuniformity $M(x)$ and camera radiometric response $r(I)$. The results all resemble Figs. 5 and 6.

B. Experiments with Real Data

Our experiments were based on the use of a Nikon D100 digital single-lens reflex camera. An advantage of this portable camera is its ability to acquire images in 12 bits by use of a linear radiometric response. Moreover, its RAW format yields data that have not undergone any processing, including white balancing. This enables us to create the effect of arbitrary radiometric response functions in 8-bit images, in postprocessing. Thus the known radiometric response is helpful for assessing the effectiveness of our calibration method. The camera exposure time and aperture were constant during the acquisition process. To create a strong vignetting effect, we attached a spatially varying optical filter to the camera lens.[47] The filter attenuation of the irradiance varied along the x axis. In our experiments we assumed that the effect of this 1D filter is much more significant than the intrinsic 2D vignetting of the lens. Hence we applied the simpler 1D analysis procedure. The solid curve in Fig. 8 shows $r^{-1}(v)$ and $M(x)$ for this system. The function $M(x)$ was calibrated in a separate process, to permit future validation.

Figure 9 shows some image frames that were acquired by us. After acquisition, the frames were registered. We then created the matrix $\mathbf{A}$ according to Eq. (25). For this purpose, we selected 6000 random pairs of corresponding pixels in different frames. Using this data, we estimated $\hat{r}^{-1}(v)$ and $\hat{M}(x)$, which are plotted by a dashed curve in Fig. 8.

Figure 10 shows two mosaics resulting from the fusion process described in Section 6. These mosaics differ only by the value K, which we assigned in their construction. The top result was based on a K value that maximized the entropy of the displayed image. The bottom result was

Fig. 10. Image mosaics constructed on the basis of real experimental data. Two different values of K were used to construct these mosaics. Seams are hardly apparent, although the original images suffered from an unknown vignetting, and the recovered vignetting and radiometric response erred by an exponential function. No dedicated seam-removal method was applied.

Fig. 11.   Image mosaic constructed by direct stitching without compensating for the radiometric response function $r(I)$ and for the optical nonuniformity $M(\mathbf{x})$.

constructed with another arbitrary K. We show these cases to demonstrate that seams are hardly apparent, even if we do not know what K is. Hence the nonuniformity was corrected such that all frames are mutually consistent. We stress again that we obtained seamless mosaicking without using any dedicated seam-removal method such as feathering. In contrast, Fig. 11 shows the image mosaic obtained without considering $\hat{M}(x)$ and $\hat{r}(I)$. Inconsistencies of the radiometric measurements create seams, since no feathering is attempted there.

8. DISCUSSION

We have presented a simple and practical method for estimating the optical nonuniformity and the radiometric response function of imaging systems. This estimation can be used for creating high-data-rate images in a wide FOV. We have demonstrated this method by experiments based on real data. We have created wide FOV image mosaics that are nearly seamless, without using dedicated techniques for seam removal. The method is not limited to nonuniformities caused by imaging optics. Rather, it can also be applied if the camera gain is nonuniform (varies across the frame FOV), while the spatial variations are gradual.

The resulting mosaics are prone to an ambiguity. This ambiguity is analogous to a fundamental ambiguity in methods that simultaneously estimate the radiometric response function and exposure ratios when multiple exposures are used.[32] We have proved that the ambiguity has the form of a γ correction. Hence our method transforms a nonparametric problem into the much simpler γ-correction operation. Interestingly, Ref. 37 presents a blind γ-correction method. Therefore it may be possible to use the method of Ref. 37 to disambiguate the solution.

We do not claim that our method makes standard methods for seam removal totally unnecessary. Those methods are of general scope and can deal with cases in which seams are not caused by camera nonuniformity but rather by scene dynamics. Nevertheless, it is demonstrated that for static scenes, seams can be mostly removed simply by addressing their root cause.

There are three directions in which this work can be extended. First, we intend to generalize the solution to systems in which the camera gain varies temporally (owing to an automatic gain-control mechanism), beyond the action of the nonlinear response and the optical nonuniformity. The second direction deals with cameras in which

$r(I)$ varies spatially in a nongradual way. In the current work, $r(I)$ is a global operation applied to all pixels. This is a good model for CCD cameras, since all pixels on the detector chip transfer their charge to a single amplifier. On the other hand, CMOS semiconductor cameras have a distinct amplifier inside each pixel, and thus the radiometric response may slightly vary between pixels. An analogous behavior occurs in thermal infrared cameras, in which each pixel may have its own radiometric response, parameterized by gain and bias.[33–36] We expect that generalizing the method to such cameras will be more challenging. Finally, a similar analysis of color pictures is a natural extension. In that case, there is a need to model the nonlinear operations performed in color spaces.

APPENDIX A: THE WEIGHT FUNCTION

To improve the performance of the algorithm described in Section 3, we increase the influence of high gray-level values. The reason is that the signal-to-noise ratio typically increases with the gray-level value. Moreover, as shown next, the influence of camera nonuniformity in high gray-level values is dominant over quantization, contrary to the situation in low gray levels. Assume that we acquire two scene points, one of which is dark and the other is bright, with corresponding image irradiances of I_{dark} and I_{bright}, respectively. Both points are acquired in two frames f_1 and f_2. In f_1, both points are measured through a region in the camera FOV for which $M=1$, leading to values $v_{\text{dark}}^{f_1}=1$ and $v_{\text{bright}}^{f_1}=100$, respectively. In f_2 both points are measured through a region in the camera FOV for which $M=0.9$. Hence in f_2 we measure $v_{\text{bright}}^{f_2}=90$. On the other hand, $v_{\text{dark}}^{f_2}=1$, rather than 0.9, owing to rounding by the quantizer. This means that Eq. (7) is strongly violated for dark scene points.

To address this problem, we define a weight function $w(v^{f_1}, v^{f_2})$, where v^{f_1} and v^{f_2} are the gray levels of the scene point in frames f_1 and f_2, respectively. The uncertainties of these values are Δv^{f_1} and Δv^{f_2}. We assume that $\Delta v^{f_1} = \Delta v^{f_2} = \sigma$, where σ is a constant (unless the pixel is saturated). Owing to the noise, Eq. (7) is violated:

$$g(v^{f_1}) - g(v^{f_2}) - l(\mathbf{x}^{f_1}) + l(\mathbf{x}^{f_2}) = 0 \pm \Delta Q(v^{f_1}, v^{f_2}), \quad \text{(A1)}$$

where ΔQ is the uncertainty of Eq. (7) due to Δv^{f_1} and Δv^{f_2}. We can express it as

$$\Delta \boldsymbol{Q}(v^{f_1}, v^{f_2}) = \sigma \left[\left(\frac{\partial \boldsymbol{Q}}{\partial v^{f_1}} \right)^2 + \left(\frac{\partial \boldsymbol{Q}}{\partial v^{f_2}} \right)^2 \right]^{1/2}. \quad \text{(A2)}$$

Thus

$$\Delta \boldsymbol{Q}(v^{f_1}, v^{f_2}) = \sigma \left\{ \left[\frac{1}{r^{-1}(v^{f_1})} \frac{\partial r^{-1}}{\partial v^{f_1}} \right]^2 + \left[\frac{1}{r^{-1}(v^{f_2})} \frac{\partial r^{-1}}{\partial v^{f_2}} \right]^2 \right\}^{1/2}. \quad \text{(A3)}$$

Assume for a moment that the radiometric response[26,37] function r is of the form $r \sim v^\gamma$. In this case,

$$\Delta \boldsymbol{Q}(v^{f_1}, v^{f_2}) = \gamma \sigma \left[\left(\frac{1}{v^{f_1}} \right)^2 + \left(\frac{1}{v^{f_2}} \right)^2 \right]^{1/2}$$

$$= \gamma \sigma \left\{ \frac{v^{f_1} v^{f_2}}{[(v^{f_1})^2 + (v^{f_2})^2]^{1/2}} \right\}^{-1}. \quad \text{(A4)}$$

The uncertainty [Eq. (A4)] increases for low gray-level values. We want to give a low weight to less reliable points. To accomplish this, we use the weight function $w(v^{f_1}, v^{f_2})$ in Eqs. (11), (24), and (25) such as $w(v^{f_1}, v^{f_2}) \propto \Delta \boldsymbol{Q}(v^{f_1}, v^{f_2})^{-1}$:

$$w(v^{f_1}, v^{f_2}) = \frac{v^{f_1} v^{f_2}}{[(v^{f_1})^2 + (v^{f_2})^2]^{1/2}}. \quad \text{(A5)}$$

This weight function increases the influence of high gray levels and decreases the influence of low gray levels in Eqs. (11), (24), and (25). Note that the development of this weight function was based on a response function of the form $r \sim v^\gamma$. Recall, however, that we generally assume no parametric knowledge of r. Hence, in general, it is not of the form $r \sim v^\gamma$. Nevertheless, we assume that the above weight function is good enough to achieve its purpose.

APPENDIX B: TWO-DIMENSIONAL LAPLACIAN OPERATOR

Let $\mathbf{B}$ be an arbitrary matrix of size $N \times N$ while $\mathbf{b}$ is a column-stack vector representation of this matrix. We should express the 2D Laplacian operator $\widetilde{\mathbf{L}}$ for the vector $\mathbf{b}$. Apparently, Eq. (10) can be written as a Toeplitz matrix. However, boundary pixels should be treated differently. The matrix $\mathbf{B}$, as depicted in Fig. 12, has two margin columns (first and last) and several internal columns. Margin columns consist of corner elements, which we call α_m, and internal elements, which we call α_i. In a similar way, each internal column β of $\mathbf{B}$ (see Fig. 12) has two marginal elements, which we call β_m (elements of the first and last rows of $\mathbf{B}$). Accounting for these boundary considerations, we find that the Laplacian operator $\widetilde{\mathbf{L}} \in \mathfrak{R}^{N^2 \times N^2}$ is a sparse matrix having five nonzero diagonals: The main diagonal is

$$\widetilde{\mathbf{L}}(n,n) = \begin{cases} -4 & \text{if } N < n < N^2 - N \text{ and } n \neq jN, jN+1, \\ & \quad j \in [1, N-1] \\ 0 & \text{if } n = 1, N, N^2 - N + 1, N^2 \\ -2 & \text{otherwise} \end{cases}, \quad \text{(B1)}$$
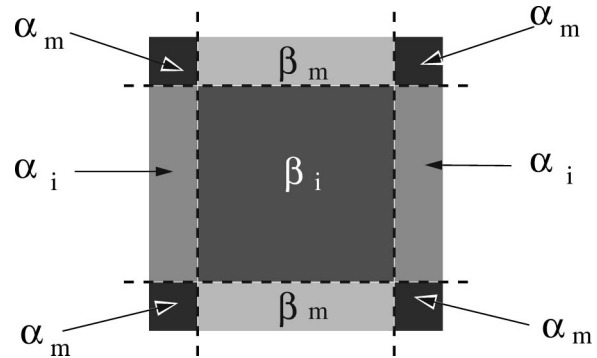
the first diagonals are

Fig. 12. Arbitrary 2D matrix $\mathbf{B}$.

$$\widetilde{\mathbf{L}}(n, n \pm 1) = \begin{cases} 1 & \text{if } n \neq jN, jN+1, j \in [0,N] \\ 0 & \text{otherwise} \end{cases}, \quad \text{(B2)}$$

and the Nth diagonals are

$$\widetilde{\mathbf{L}}(n, n \pm N) = \begin{cases} 1 & \text{if } N < n \leq N^2 - N \\ 0 & \text{otherwise} \end{cases}. \quad \text{(B3)}$$

REFERENCES AND NOTES

1. S. B. Kang and R. Weiss, "Can we calibrate a camera using an image of a flat, textureless Lambertian surface?" in *Proceedings of European Conference on Computer Vision*, (Springer, New York, 2000), Part 2, pp. 640–653.
2. I. C. Khoo, M. V. Wood, M. Y. Shih, and P. H. Chen, "Extremely nonlinear photosensitive liquid crystals for image sensing and sensor protection," Opt. Express **4**, 432–442 (1999).
3. N. Tabiryan and S. Nersisyan, "Liquid-crystal film eclipses the sun artificially," Laser Focus World **38**, 105–108 (2002).
4. In different communities the terms mosaicing[5,6] and mosaicking[7-10] are used.
5. D. Capel and A. Zisserman, "Automated mosaicing with super-resolution zoom," in *Proceedings of IEEE Conference on Computer Vision and Pattern Recognition* (IEEE Press, Piscataway, N.J., 1998), pp. 885–891.
6. S. Peleg, M. Ben-Ezra, and Y. Pritch, "Omnistereo: panoramic stereo imaging," IEEE Trans. Pattern Anal. Mach. Intell. **23**, 279–290 (2001).
7. R. Kwok, J. C. Curlander, and S. Pang, "An automated system for mosaicking spaceborne SAR imagery," Int. J. Remote Sens. **11**, 209–223 (1990).
8. R. Eustice, O. Pizarro, H. Singh, and J. Howland, "UWIT: Underwater Image Toolbox for optical image processing and mosaicking in MATLAB," in *Proceedings of IEEE*

International Symposium on Underwater Technology (IEEE Press, Piscataway, N.J., 2002), pp. 141–145.

9. R. Garcia, J. Batlle, X. Cufi, and J. Amat, "Positioning an underwater vehicle through image mosaicking," in *Proceedings of IEEE International Conference on Robotics and Automation* (IEEE Press, Piscataway, N.J., 2001), Part 3, pp. 2779–2784.

10. M. L. Duplaquet, "Building large image mosaics with invisible seam lines," in Visual Information Processing VII, S. K. Park and R. D. Juday, eds., Proc. SPIE **3387**, 369–377 (1998).

11. C. J. Lada, D. L. DePoy, K. M. Merrill, and I. Gatley, "Infrared images of M17," Astron. J. **374**, 533–539 (1991).

12. L. A. Soderblom, K. Edwards, E. M. Eliason, E. M. Sanchez, and M. P. Charette, "Global color variations on the Martian surface," Icarus **34**, 446–464 (1978).

13. J. M. Uson, S. P. Boughn, and J. R. Kuhn, "The central galaxy in Abell 2029: an old supergiant," Science **250**, 539–540 (1990).

14. A. R. Vasavada, A. P. Ingersoll, D. Banfield, M. Bell, P. J. Gierasch, and M. J. S. Belton, "Galileo imaging of Jupiter's atmosphere: the great red spot, equatorial region, and white ovals," Icarus **135**, 265–275 (1998).

15. S. Negahdaripour, X. Xu, A. Khemene, and Z. Awan, "3-D motion and depth estimation from sea-floor images for mosaic-based station-keeping and navigation of ROV's/ AUV's and high-resolution sea-floor mapping," in *Proceedings of IEEE Workshop on Autonomous Underwater Vehicles* (IEEE Press, Piscataway, N.J., 1998), pp. 191–200.

16. M. Hansen, P. Anandan, K. Dana, G. van der Wal, and P. Burt, "Real-time scene stabilization and mosaic construction," in *Proceedings of IEEE Workshop on Applications of Computer Vision* (IEEE Press, Piscataway, N.J., 1994), pp. 54–62.

17. E. M. Reynoso, G. M. Dubner, W. M. Goss, and E. M. Arnal, "VLA observations of neutral hydrogen in the direction of Puppis A," Astron. J. **110**, 318–324 (1995).

18. P. J. Burt and E. H. Adelson, "A multiresolution spline with application to image mosaics," ACM Trans. Graphics **2**, 217–236 (1983).

19. A. Levin, A. Zomet, S. Peleg, and Y. Weiss, "Seamless image stitching in the gradient domain," in *Proceedings of European Conference in Computer Vision* (Springer, New York, 2004), Part IV, pp. 377–390.

20. H. Y. Shum and R. Szeliski, "Systems and experiment paper: construction of panoramic image mosaics with global and local alignment," Int. J. Comput. Vision **36**, 101–130 (2000).

21. M. Aggarwal and N. Ahuja, "High dynamic range panoramic imaging," in *Proceedings of IEEE International Conference on Computer Vision* (IEEE Press, Piscataway, N.J., 2001), Vol. I, pp. 2–9.

22. Y. Y. Schechner and S. K. Nayar, "Generalized mosaicing," in *Proceedings of IEEE International Conference on Computer Vision* (IEEE Press, Piscataway, N.J., 2001), Vol. I, pp. 17–24.

23. Y. Y. Schechner and S. K. Nayar, "Generalized mosaicing: high dynamic range in a wide field of view," Int. J. Comput. Vision **53**, 245–267 (2003).

24. P. E. Debevec and J. Malik, "Recovering high dynamic range radiance maps from photographs," in *Proceedings of SIGGRAPH 97* (Association for Computing Machinery, New York, 1997), pp. 369–378.

25. S. Mann and R. W. Picard, "On being 'undigital' with digital cameras: extending dynamic range by combining differently exposed pictures," in *Proceedings of IS&T 48th Annual Conference* (Society for Imaging Science and Technology, Springfield, Va., 1995), pp. 422–428.

26. S. Mann, "Comparametric equations with practical applications in quantigraphic image processing," IEEE Trans. Image Process. **9**, 1389–1406 (2000).

27. T. Mitsunaga and S. K. Nayar, "Radiometric self calibration," *Proceedings of IEEE Conference on Computer Vision and Pattern Recognition* (IEEE Press, Piscataway, N.J., 1999), Vol. I, pp. 374–380.

28. S. J. Kim and M. Pollefeys, "Radiometric alignment of image sequences," in *Proceedings of IEEE Conference on Computer Vision and Pattern Recognition* (IEEE Press, Piscataway, N.J., 2004), Vol. I, pp. 645–652.

29. J. Jia and C. K. Tang, "Image registration with global and local luminance alignment," in *Proceedings of IEEE Conference on Computer Vision* (IEEE Press, Piscataway, N.J., 2003), Vol. I, pp. 156–163.

30. F. M. Candocia, "Jointly registering images in domain and range by piecewise linear comparametric analysis," IEEE Trans. Image Process. **12**, 409–419 (2003).

31. S. Mann and R. Mann, "Quantigraphic imaging: estimating the camera response and exposures from differently exposed images," in *Proceedings of IEEE Conference on Computer Vision and Pattern Recognition* (IEEE Press, Piscataway, N.J., 2001), Vol. 1, pp. 842–849.

32. M. D. Grossberg and S. K. Nayar, "Determining the camera response from images: what is knowable?," IEEE Trans. Pattern Anal. Mach. Intell. **25**, 1455–1467 (2003).

33. P. Törle, "Scene-based correction of image sensor deficiencies," MSc. thesis (Linköping Institute of Technology, Linköping, Sweden, 2003).

34. R. C. Hardie, M. M. Hayat, E. Armstrong, and B. Yasuda, "Scene-based nonuniformity correction with video sequences and registration," Appl. Opt. **39**, 1241–1250 (2000).

35. B. M. Ratliff, M. M. Hayat, and J. S. Tyo, "Radiometrically accurate scene-based nonuniformity correction for array sensors," J. Opt. Soc. Am. A **20**, 1890–1899 (2003).

36. S. N. Torres, J. E. Pezoa, and M. Hayat, "Scene-based nonuniformity correction for focal plane arrays by the method of the inverse covariance form," Appl. Opt. **42**, 5872–5881 (2003).

37. H. Farid, "Blind inverse gamma correction," IEEE Trans. Image Process. **10**, 1428–1433 (2001).

38. S. Lin, J. Gu, S. Yamazaki, and H. Shum, "Radiometric calibration from a single image," in *Proceedings of IEEE Conference on Computer Vision and Pattern Recognition* (IEEE Press, Piscataway, N.J., 2004), Vol. II, pp. 938–946.

39. S. Inoue, *Video Microscopy* (Plenum, New York, 1986). pp. 209–214.

40. The radiometric response function is usually monotonically increasing. It monotonically decreases in negative films and in some camera modes.

41. S. Hsu, H. S. Sawhney, and R. Kumar, "Automated mosaics via topology inference," IEEE Comput. Graphics Appl. **22**, 44–54 (2002).

42. M. Irani, P. Anandan, J. Bergen, R. Kumar, and S. Hsu, "Efficient representations of video sequences and their application," Signal Process. **8**, 327–351 (1996).

43. R. K. Sharma and M. Pavel, "Multisensor image registration," in *Proceedings of the Society for Information Display* (Society for Information Display, Playa del Ray, Calif., 1997), Vol. XXVIII, pp. 951–954 (1997).

44. P. Thevenaz and M. Unser, "Optimization of mutual information for multiresolution image registration," IEEE Trans. Image Process. **9**, 2083–2099 (2000).

45. P. Viola and W. M. Wells III, "Alignment by maximization of mutual information," Int. J. Comput. Vision **24**, 137–154 (1997).

46. We may avoid the apperance of trivial solution by expressing Eq. (15) in a matrix formulation. This is only one of the possible realizations of the requirement to avoid a nontrivial g. Another possibility is to fix the boundary range values of g.

47. We placed the filter a few centimeters ahead of the lens. If the filter is placed right next to the lens, it affects the aperture properties[48] without producing spatially varying effects in the image.

48. H. Farid and E. P. Simoncelli, "Range estimation by optical differentiation," J. Opt. Soc. Am. A **15**, 1777–1786 (1998).